

Freeze-out configuration properties in the $^{197}\text{Au} + ^{197}\text{Au}$ reaction at 23 AMeV

R.Najman,¹ R.Łaneta,^{1,*} A. Sochocka,² F.Amorini,^{3,4} L.Auditore,⁵ T.Cap,⁶ G.Cardella,⁷ E. De Filippo,⁷ E.Geraci,^{4,7} A.Grzeszczuk,⁸ S.Kowalski,⁸ T.Kozik,¹ G.Lanzalone,^{3,9} I.Lombardo,^{10,11} Z. Majka,¹ N.G.Nicolis,¹² A.Pagano,⁷ E.Piasecki,^{13,14} S.Pirrone,⁷ G.Politi,^{4,7} F.Rizzo,^{3,4} P.Russotto,⁷ K.Siwiek-Wilczyńska,⁶ I.Skwira-Chalot,⁶ A.Trifiro,¹⁵ M.Trimarchi,¹⁵ J.Wilczyński,¹⁴ and W.Zipper⁸

¹*M.Smoluchowski Institute of Physics, Jagiellonian University, Kraków, Poland*

²*Department of Physics, Astronomy and Applied Informatics, Jagiellonian University, Kraków, Poland*

³*INFN, Laboratori Nazionali del Sud, Catania, Italy*

⁴*Dipartimento di Fisica e Astronomia Università di Catania, Catania, Italy*

⁵*Dipartimento di Fisica e Scienze della Terra Università di Messina and INFN Gruppo Collegato di Messina, Italy*

⁶*Faculty of Physics, University of Warsaw, Warsaw, Poland*

⁷*INFN, Sezione di Catania, Italy*

⁸*Institute of Physics, University of Silesia, Katowice, Poland*

⁹*Università degli Studi di Enna "Kore", Enna, Italy*

¹⁰*Dip. di Fisica, Università di Napoli Federico II, Naples, Italy*

¹¹*INFN, Sezione di Napoli, Italy*

¹²*Department of Physics, The University of Ioannina, Ioannina, Greece*

¹³*Heavy Ion Laboratory, University of Warsaw, Warsaw, Poland*

¹⁴*National Centre for Nuclear Research, Otwock-Świerk, Poland*

¹⁵*Dipartimento di Fisica Università di Messina and INFN Gruppo Collegato di Messina, Italy*

(Dated: July 30, 2018)

Data from the experiment on the $^{197}\text{Au} + ^{197}\text{Au}$ reaction at 23 AMeV are analyzed with an aim to find signatures of exotic nuclear configurations such as toroid-shaped objects. The experimental data are compared with predictions of the ETNA code dedicated to look for such configurations and with the QMD model. A novel criterion of selecting events possibly resulting from the formation of exotic freeze-out configurations, "the efficiency factor", is tested. Comparison between experimental data and model predictions may indicate for the formation of flat/toroidal nuclear systems.

PACS numbers: 25.70.Gh, 25.70.Pq

I. INTRODUCTION

The search for exotic nuclear configurations was inspired by J.A.Wheeler [1]. His idea was investigated by many authors who studied the stability of exotic nuclear shapes (see e.g. [2–4]). Theoretical investigations have shown that very exotic extra superheavy nuclei can be reached only if non-compact shapes are taken into account. Calculations for bubble structures showed that such nuclei can be stable for $Z > 240$ and $N > 500$ (see e.g. [5–7]). Recently it was found that for nuclei with $Z > 140$ the global energy minimum corresponds to toroidal shapes [8, 9]. In contrast to bubble nuclei, the synthesis of toroidal nuclei is experimentally available in collisions between stable isotopes.

To address this issue simulations were performed for Au + Au collisions in a wide range of incident energies using the BUU code [10, 11]. These calculations indicate that the threshold energy for the formation of toroidal nuclear shapes is located around 23 AMeV.

Also Improved Quantum Molecular Dynamics Model calculations performed for U + U collisions have shown

a possible formation of toroidal freeze-out configurations above a specific collision energy for this heavy system [12]. Such toroidal-shape complex can be also created in macroscale in binary droplet collisions above some threshold velocity [13].

A number of observables were suggested as the signatures of noncompact freeze-out configurations. These were:

- Larger number of intermediate mass fragments should be observed than would be expected for the decay of a compact object;
- Enhanced similarity in the charge and size of the fragments should also be observed;
- Suppressed sphericity in the emission of fragments should be visible.

The simulations of decay process of different break up configurations using the ETNA code were performed to study the ability of the CHIMERA detector [14, 15] for recognition of non-compact configurations. Analysis of different observables have shown that a quantity named "the efficiency factor" of events with 5 heavy fragments can be used as a criterion of selecting events possibly resulting from formation of toroidal configurations [16, 17].

* E-Mail:roman.planeta@uj.edu.pl

The CHIMERA collaboration has carried out an experiment on the $^{197}\text{Au} + ^{197}\text{Au}$ reaction at 23 AMeV energy, focused on two independent goals, first on the extension of the earlier study at lower energy of 15 AMeV, in which a new reaction mechanism of violent breakup of non-fusing $^{197}\text{Au} + ^{197}\text{Au}$ system into 3 and/or 4 massive fragments was observed [18], [19], [20], and second, on the search of exotic nuclear configurations such as toroidal shapes. Some preliminary results of the former project have been published in [21].

In this work we report results of our analysis focused on the question of exotic configurations involving the breakup of the $^{197}\text{Au} + ^{197}\text{Au}$ system into 5 or more fragments. The experimental data are compared with model predictions. Conclusions regarding the shape of the freeze-out configuration are drawn.

This paper is organized as follows. In Sec. 2 we present the experiment and data calibration procedures. General characteristics of experimental data are shown in Sec. 3. The dedicated observables are discussed in Sec. 4. The conclusions are presented in Sec. 5.

II. EXPERIMENT AND DATA CALIBRATION PROCEDURE

The experiment for the $^{197}\text{Au} + ^{197}\text{Au}$ reaction at 23 AMeV was performed at INFN-LNS Superconducting Cyclotron of Catania. During the experiment two gold targets were used: 164 and 396 $\mu\text{g}/\text{cm}^2$. The thinner target was used in calibration measurements and the thicker one in the production runs. Reaction products were detected with the CHIMERA multidetector [14, 15] that is constituted by 1192 telescopes arranged in 35 rings in full 2π azimuthal symmetry around the beam axis, covering the polar angle between 1° and 176° . A single detection cell is constituted of a planar n-type silicon detector ($\cong 300 \mu$ thickness) followed by a Cs(Tl) scintillator of thickness varying from 12 cm at forward angles to 3 cm at backward angles.

The collected data were calibrated using a set of dedicated programs developed at INFN-LNS. Energy calibration of Si detectors was performed using ion beams, delivered both by the tandem and the cyclotron. Data for the following systems were used: (i) the elastic scattering data for $^{16}\text{O} + \text{Au}$ at 60 and 80 MeV, $^{58}\text{Ni} + \text{Au}$ at 142 MeV, $\text{Au} + \text{Au}$ at 170 MeV and 23 AMeV; (ii) recoil peak for $\text{Au} + ^{12}\text{C}$ at 170 MeV; and (ii) fission fragments from $\text{Au} + ^{12}\text{C}$ reaction at 23 AMeV. Unlike in the analysis of ternary breakup reactions [21] in which the pulse-height defect was calculated with the formula of Ref. [22], in the present analysis the pulse-height defect in silicon detectors was calculated using the same procedure as described in Ref. [23].

In order to identify fragments two methods were applied: (i) the $\Delta E - E$ technique for fragments punching through the silicon detectors; (ii) the time of flight (TOF) method for the class of fragments stopped in Si

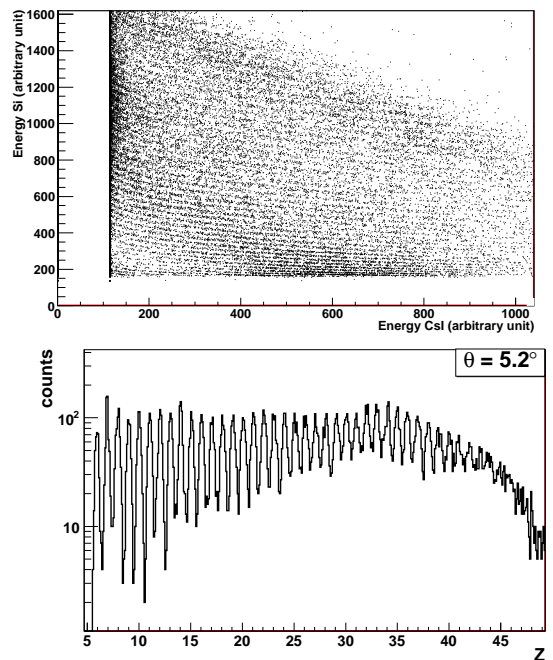


FIG. 1: $\Delta E - E$ spectrum (upper panel) and the corresponding Z spectrum (bottom panel) for fragments detected in telescope placed at $\theta = 5.2^\circ$ for $\text{Au} + \text{Au}$ reaction at 23 AMeV.

detectors. In Fig. 1 (upper part) an example of $\Delta E - E$ plot is shown for a detector belonging to the 3-th internal ring, at a polar angle $\theta = 5.2^\circ$. The Z distribution of fragments identified by the $\Delta E - E$ method for the same detector is presented also in Fig. 1 (bottom panel). We can see that in the Z spectrum a good charge identification can be observed up to $Z = 42$. At this angular range one observes a broad maximum of the charge distribution located at charges $Z = 30 - 40$ corresponding to Au fission fragments. One observes also a substantial contribution of lighter fragments. In order to estimate a missing information on mass of the fragments identified in charge by $\Delta E - E$ method, the EPAX formula [24–26] was used.

The mass of fragments stopped in Si detector is determined by TOF method. The start signal was given by 30% Constant Fraction Discriminator acting on time signal generated by the silicon detector, while the stop signal was given by delayed Reference Signal delivered by cyclotron. Examples of $\Delta E - \text{TOF}$ spectra are presented in Fig. 2. In this case mass values are calculated using the formula:

$$m = 2E \cdot (t_0 - t)^2 / R^2, \quad (1)$$

where R is the distance between the target and a given detector and the t_0 is a time offset of the measured time t .

A crucial problem in the calibration of TOF measurements for the CHIMERA multidetector is evaluation of

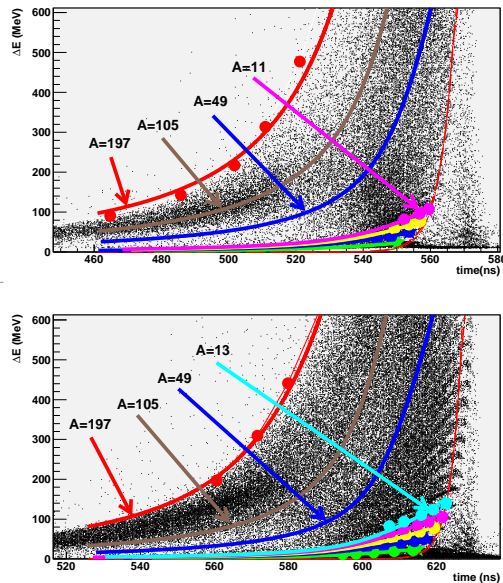


FIG. 2: (color online) The $\Delta E - TOF$ distributions for detectors 404 (upper panel) and 653 (bottom panel) located at $\theta = 17^\circ$ and 28.5° , respectively. Lines presented of both figures correspond to positions of masses as indicated.

t_0 offset that must be determined for each detector individually. Moreover, t_0 depends on mass, charge and kinetic energy of the detected fragment. The t_0 values for well identified light fragments and Au-like nuclei fragments located at the left-hand-side edge of the $\Delta E - TOF$ distribution (see Fig. 2) are presented by color symbols in Fig. 3. For relatively light fragments a well tested parametrization of t_0 for CHIMERA detectors was proposed [27]. To calibrate t_0 for medium and heavy fragments in $^{197}\text{Au} + ^{197}\text{Au}$ experiments a new calibration method based on a functional dependence of t_0 on mass, charge and pulse-height-defect dependent kinetic energy was developed (see e.g. [28]) and applied in analysis of the ternary breakup experiment [21].

In the present analysis we use another method of the parametrization of t_0 offset:

$$t_0 = \begin{cases} t_{0,sat} & t_{0,sat} < \Delta t \\ t_{0,sat} - \Delta t & t_{0,sat} > \Delta t \end{cases} \quad (2)$$

$$\Delta t = B - A(1 - \exp(\gamma \cdot m)) \cdot \left(\frac{E}{E_{PT}}\right)^{(\alpha - \delta \cdot m)} \cdot \exp\left[-\left(\frac{E + (\beta + \mu \cdot m)E_{PT}}{E_{PT}}\right)^\epsilon\right], \quad (3)$$

where $t_{0,sat}$ is determined for particles punching through the silicon detector. The E_{PT} is the highest energy deposited by particles with mass m .

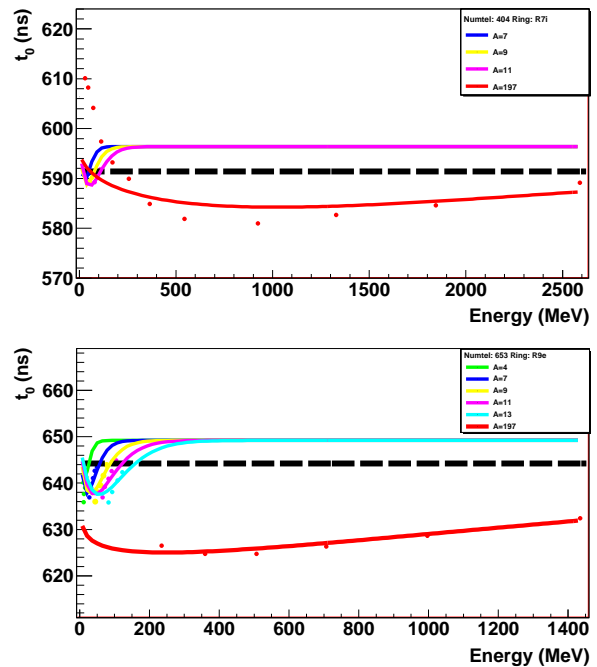


FIG. 3: (color online) The t_0 dependence on incident energy and particle mass for telescopes 404 and 653 located at $\theta = 17^\circ$ and 28.5° , respectively. Color symbols represent the t_0 values for identified light fragments and Au-like fragments. Solid lines represent the fitting results using the formula. The dashed line indicate the $t_{0,sat}$ value.

The values of the parameters A , B , α , β , γ , μ and ϵ were determined by fitting Eq. (2) to selected points for well identified light fragments and Au-like nuclei fragments (see Fig. 3). In this procedure fragment energies were corrected for pulse-height defect and their Z values were estimated using the EPAX formula [22-24]. Fig. 3 presents the t_0 calibration lines calculated for selected mass values. The calculated positions in the $\Delta E - TOF$ distributions for some selected mass numbers are shown for two detectors in Fig. 2 as solid color lines.

In Fig. 4 two dimensional mass versus kinetic energy distributions are shown for telescopes located at two angular regions. For $3^\circ < \theta < 10^\circ$ region (upper panel) the distribution extends from small masses seen at low energies up to the Au elastic peak. For $20^\circ < \theta < 29^\circ$ region (bottom panel) the particles with masses up to 200 a.m.u. are observed at relatively low kinetic energies.

III. THE GENERAL CHARACTERISTICS OF EXPERIMENTAL DATA

In Fig. 5 two dimensional distribution mass versus parallel velocity of identified fragments is shown. Location of quasielastic Au peak is visible at mass around 200 and velocities close to the beam velocity ($v_p = 6.67\text{cm/ns}$).

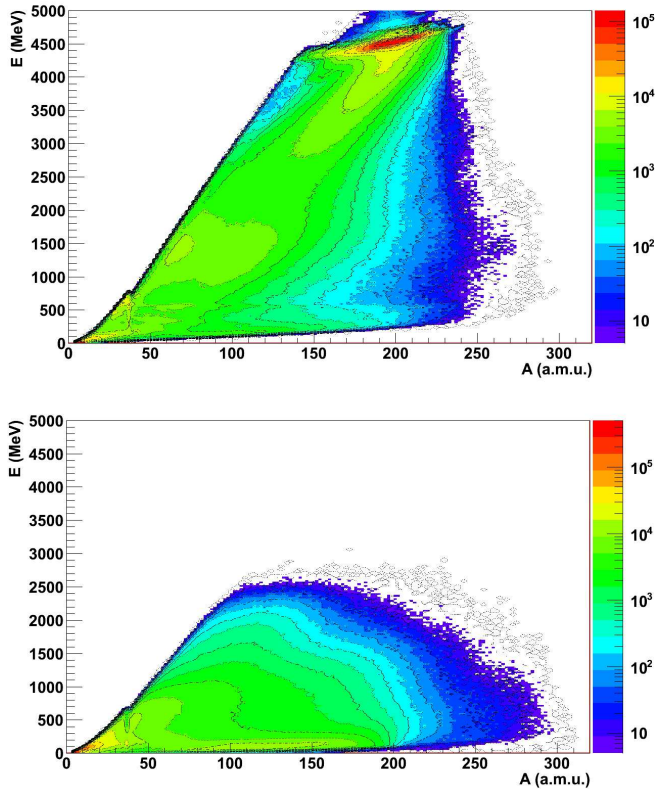


FIG. 4: (color online) The correlation between mass and energy for fragments observed in telescopes located at $3^\circ < \theta < 10^\circ$ (upper panel), and $20^\circ < \theta < 29^\circ$ (bottom panel).

Peak corresponding to Au recoil fragments can be found at velocities close to zero. Here one can observe an underestimation of mass value for these fragments due to the imperfection of used t_0 parametrizations (see Eq. 2). At velocities between these two limits fragments originating from fission of the Au-like nuclei are located. One can also identify a separated region located at low masses and velocity close to center of mass velocity. This region correspond to the intermediate velocity source.

For the registered events we have constructed the plot presenting the dependence between the total charge of identified fragments, Z_{tot} , versus total parallel momentum of those fragments normalized to the beam momentum, $p_{||,tot}/p_{proj}$ (see Fig. 6).

One can distinguish different regions on this plot. In the region of low values of total collected charge and low parallel momentum one observes the ridge corresponding to the badly detected events. In the region of total parallel momentum close to 1 and total collected charge close to the charge of projectile one observes the maximum corresponding to deep inelastic collisions where the target like fragment remains undetected. Region where the total detected charge is close to total charge of the system

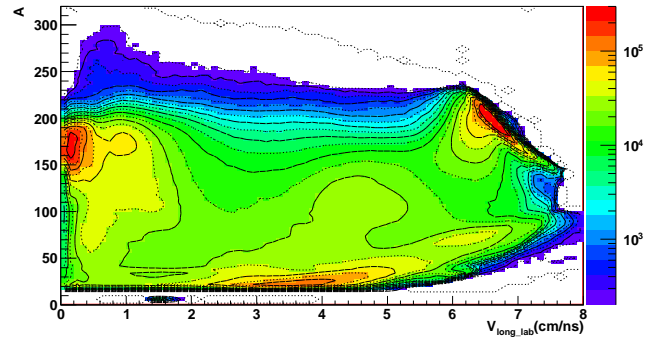


FIG. 5: (color online) The correlation between mass of identified fragments versus parallel velocity of those fragments.

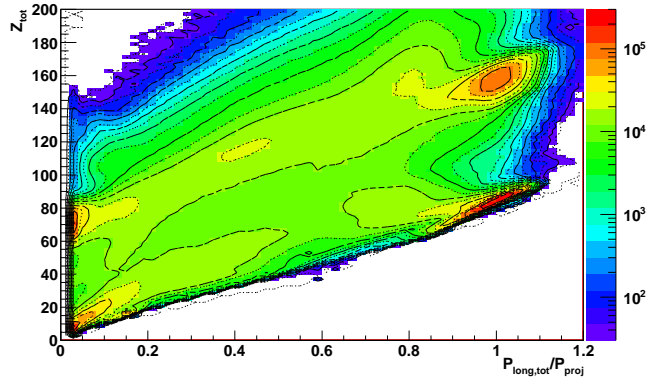


FIG. 6: (color online) The correlation between total charge of identified fragments versus total parallel momentum of those fragments normalized to the beam momentum.

and the total parallel linear momentum is close to linear momentum of the projectile can be called as region of well reconstructed events. In our present analysis this region is selected imposing the conditions: $120 < Z_{tot} < 180$ and $0.8 < p_{||,tot}/p_{proj} < 1.1$. The number of events fulfilling these conditions is equal $5.9 * 10^6$.

For this class of well reconstructed events in the Au + Au reaction the multiplicity distribution of fragments with charge $Z_{frag} \geq 3$ and $Z_{frag} \geq 10$ are presented in Fig. 7. One can notice here that the number of events with five or more fragments corresponding to above charge thresholds is equal about 116 000 and 6 000, respectively.

IV. DATA ANALYSIS

Based on results of Ref. [18], [19] and [20], in analysis of ternary and quaternary events one expects the ob-

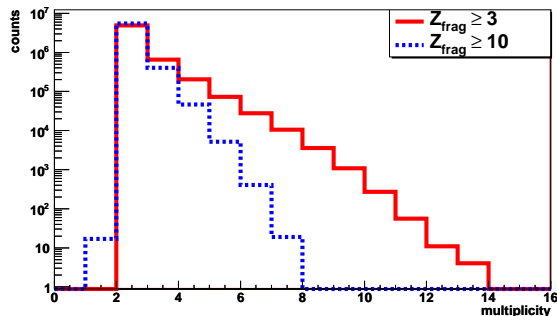


FIG. 7: (color online) Multiplicity distributions of fragments with $Z_{frag} \geq 3$ (red histogram) and $Z_{frag} \geq 10$ (blue histogram), respectively.

ervation of binary deep-inelastic collisions followed by breakup of one or both primary reaction products. Results of analysis of this particular class of reactions can be found in [21].

For the class of events with five fragments one can consider at least two mechanisms responsible for the presence of the fifth heavy fragment: (i) creation of the fragment in the interaction region (intermediate velocity source) for peripheral collisions or (ii) the multifragmentation of the composite nuclear system formed in central collisions.

In order to investigate the reaction scenario responsible for events with five and more fragments we have compared experimental data with ETNA and QMD model predictions. The ETNA model can simulate the decay of nuclear system assuming compact and noncompact freeze out configurations [16]. In this model three freeze out configurations are considered: (i) ball geometry with volume 3 and 8 times greater than normal nuclear volume V_0 (fragments uniformly distributed inside the sphere); (ii) fragments distributed on the surface of the sphere mentioned above (bubble configuration); (iii) fragments distributed on the ring with diameter 12 fm and 15 fm (toroidal configuration). In this model we consider events corresponding to central collisions only (0-3 fm impact parameter range).

In order to simulate the contribution from noncentral collisions the QMD model [29] calculations were performed in the full impact parameter range 0 - 12 fm. In our analysis the QMD code developed by Lukasik et al. [30] was used. This code takes into account: (i) protons and neutrons (in standard QMD each nucleon has an effective Z/A charge); (ii) momentum dependent Pauli potential (Skyrme + Coulomb + Symmetry + Surface + Pauli) is used instead of the Yukawa potential; (iii) initial nuclei in their real ground states with minimum energy (thanks to the Pauli potential) are prepared, (iv) strict angular momentum conservation in collisions is applied; (v) to simulate the Pauli blocking: in Lukasik code the overlap of 6-dimensional Gaussians is used, unlike in standard QMD where overlap of appropriate spheres in

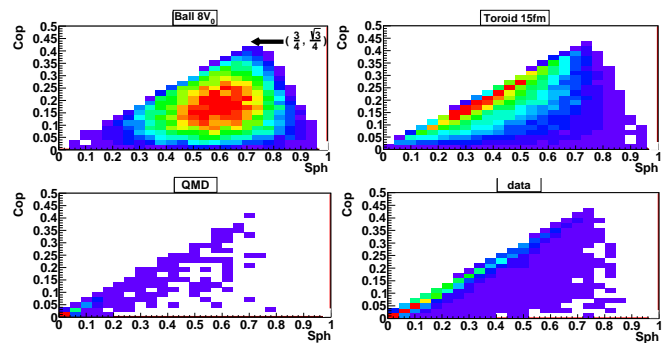


FIG. 8: (color online) The coplanarity vs sphericity distributions for Ball $8V_0$, Toroid 15 fm, QMD and experimental data.

configuration and momentum space is included.

A. The shape sensitive observables

In our analysis several observables sensitive to the freeze-out break-up configuration are investigated. As a first, we consider the shape of events in the momentum space [31]. The diagonalization of the momentum tensor gives three eigenvalues λ_i and three eigenvectors \vec{e}_i . The sphericity and coplanarity variables are defined as:

$$s = 1.5(1 - \lambda_1), c = \frac{\sqrt{3}}{2}(\lambda_2 - \lambda_3), \quad (4)$$

where $\lambda_1 > \lambda_2 > \lambda_3$ are normalized to their sum.

In the coplanarity vs sphericity plane all events are located inside a triangle defined by points $(0,0)$, $(\frac{3}{4}, \frac{\sqrt{3}}{4})$, and $(1,0)$. In Fig. 8 the (s,c) distribution for experimental data is compared to the ETNA model predictions for Ball $8V_0$, Toroid 15 fm freezeout decay configurations and with QMD predictions. In the case of ball geometry the maximum of the corresponding distribution is located in the centre of the triangle. For toroidal configuration the distribution is located closer to the line $(0,0)$, $(\frac{3}{4}, \frac{\sqrt{3}}{4})$. One can see that the experimental distribution looks very similar to QMD distribution which is dominated by noncentral collisions contribution.

In order to reduce noncentral contribution we have investigated for the QMD model predictions the dependence between flow angle, θ_{flow} , and impact parameter (see Fig. 9 (panel a), where θ_{flow} is the angle between beam axis and the eigenvector \vec{e}_1 for the largest eigenvalue λ_1). One can see on this plot that most noncentral events are located at small θ_{flow} angles. The similar dependence is observed for experimental data between θ_{flow} and total transverse momentum, p_{trans} , used as impact parameter estimator (see Fig. 9 (panel c)). We decide to reduce contribution of noncentral events both

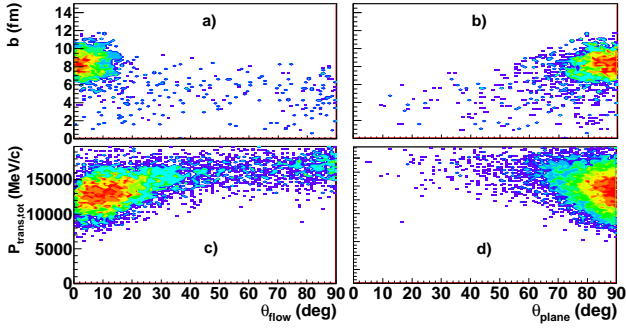


FIG. 9: (color online) The impact parameter vs θ_{flow} dependence for QMD model predictions (panel a) and total transverse momentum, p_{trans} , vs θ_{flow} dependence for experimental data (panel c). The impact parameter vs θ_{plane} dependence for QMD model predictions (panel b) and total transverse momentum, p_{trans} , vs θ_{plane} dependence for experimental data (panel d).

for experimental data and model predictions by using the condition $\theta_{flow} > 20^\circ$.

The δ , and Δ^2 observables as most sensitive to the shape of freeze out configurations were selected [16]. The δ variable is related to sphericity and coplanarity variables. The δ variable measures the distance between a given point of the (s,c) distribution and the line defined by points $(0,0)$, $(\frac{3}{4}, \frac{\sqrt{3}}{4})$. In the Fig. 10 (left panels) the δ distributions are presented for experimental data, ETNA model predictions for considered freeze-out geometries and QMD predictions. One can see here that the δ distribution for experimental data is similar to that corresponding QMD predictions. The biggest difference can be observed with the distribution for Ball $8V_0$ configuration.

The Δ^2 variable used in our analysis gives a measure of the event flatness in the velocity space. For each event we are establishing the plane in the velocity space. The parameters of this plane are selected in the way that the sum of squares of distances between the plane and the endpoints $(v_{x,i}, v_{y,i}, v_{z,i})$ of velocity vectors reach the minimum value. This last quantity is called the Δ^2 parameter and is defined as:

$$\Delta^2 = \min \left[\sum_{i=1}^{N_{fr}} (d_i^2(A, B, C, D)) \right], \quad (5)$$

where:

$$d_i = \frac{|A \cdot v_{x,i} + B \cdot v_{y,i} + C \cdot v_{z,i} + D|}{\sqrt{A^2 + B^2 + C^2}}, \quad (6)$$

and parameters A, B, C, and D are the plane parameters. The plane parameters and the velocities of fragments are in the velocity of light units.

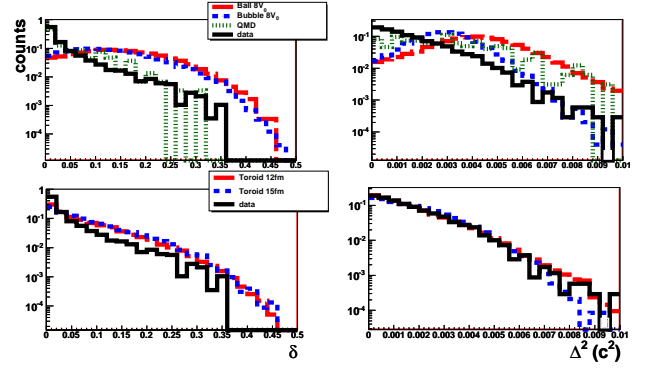


FIG. 10: (color online) In the upper left panel the δ distributions are presented for experimental data, Ball $8V_0$, Bubble $8V_0$ freeze-out geometries and QMD predictions. In the bottom left panel the experimental distribution is compared with predictions for Toroid 12 fm and Toroid 15 fm configurations. In the right panels the Δ^2 distributions for experimental data and model predictions are shown. All the distributions presented here are constructed using the condition $Z_{frag} \geq 10$ and $\theta_{flow} > 20^\circ$.

The Δ^2 distributions are shown in Fig. 10 (right panels) for data and model predictions. One can see here that for Δ^2 variable the biggest difference between experimental distribution and model predictions is observed for the Ball $8V_0$, and Bubble $8V_0$ configurations. In contrast to that, the experimental data seem to be more consistent with the simulations assuming toroidal freeze-out configurations.

In relation with Δ^2 parameter one can define an angle, θ_{plane} , between the beam direction and vector normal to the plane defined by parameters A, B, C, and D. For events corresponding to noncentral collisions, where most of reaction products are located in the reaction plane, θ_{plane} should be close to 90° . This behavior is illustrated in Fig. 9 (panel b) for QMD model predictions, where most of noncentral events are located in the reaction plane. The similar dependence is observed for experimental data between θ_{flow} and total transverse momentum, p_{trans} , used as impact parameter estimator (see panel d).

The dependence between θ_{plane} and θ_{flow} for Ball $8V_0$, Toroid 15 fm, QMD and experimental data is presented in Fig. 11. One observe here that for experimental data most of events is located in the region selected by conditions $\theta_{flow} < 20^\circ$ and $\theta_{plane} > 75^\circ$. The same behavior is observed in the case of QMD calculations. These observations indicate that such events correspond to noncentral collisions. For the Ball $8V_0$ configuration one observes the correlation between θ_{flow} and θ_{plane} angles. For toroidal configuration the correlation between these angles is even stronger. Most of these events is located in the region defined by conditions $\theta_{flow} > 20^\circ$ and $\theta_{plane} < 75^\circ$.

Following the method proposed in Ref. [16] we select

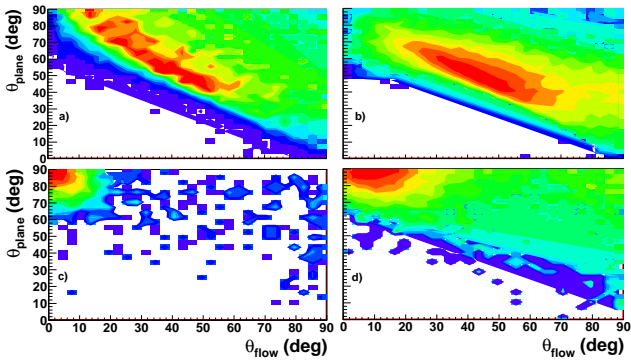


FIG. 11: (color online) The dependence between θ_{plane} and θ_{flow} for Ball $8V_0$ (panel a), Toroid 15 fm (panel b), QMD (panel c) and experimental data (panel d).

events corresponding to a toroidal shape by the set of conditions:

$$\Delta^2 < 0.001 c^2 \text{ and } \delta < 0.05. \quad (7)$$

As an efficiency measure of the above conditions we take ratio of number of events fulfilling the selection conditions to the number of events with five and more heavy fragments. Hereafter, this ratio is called the efficiency factor (EF).

The results of this procedure are presented in the Fig. 12 for different regions of θ_{flow} and θ_{plane} angles. As one can see the EF is very low for spherical freeze-out configurations with respect to the corresponding values for toroidal configurations.

For QMD calculations the value of the efficiency factor is strongly dependent on the θ_{plane} range. The condition $\theta_{plane} < 75^\circ$ reduces the number of flat noncentral events mostly located in the reaction plane. For events selected additionally by the condition $\theta_{flow} < 20^\circ$ the EF drops to zero.

For experimental data the value of the efficiency factor is about 50% for events located in the reaction plane ($\theta_{plane} > 75^\circ$) and is reduced by factor of 2 for events perpendicular to the reaction plane. These values are weakly dependent on the θ_{flow} angle range.

One observes that the values of the EF for experimental data are much larger than the corresponding predictions for QMD model. The biggest difference is observed for events located outside the reaction plane ($\theta_{plane} < 75^\circ$) at small θ_{flow} angles.

In order to investigate a possible formation of toroidal configurations in our analysis we selected the region where according to ETNA predictions the toroidal configuration is most pronounced in the θ_{flow} and θ_{plane} plane ($\theta_{plane} < 75^\circ$ and $\theta_{flow} > 20^\circ$). In Table I the efficiency factor values are given for experimental data and model predictions. The efficiency factor values are shown for four threshold values of the fragment charge.

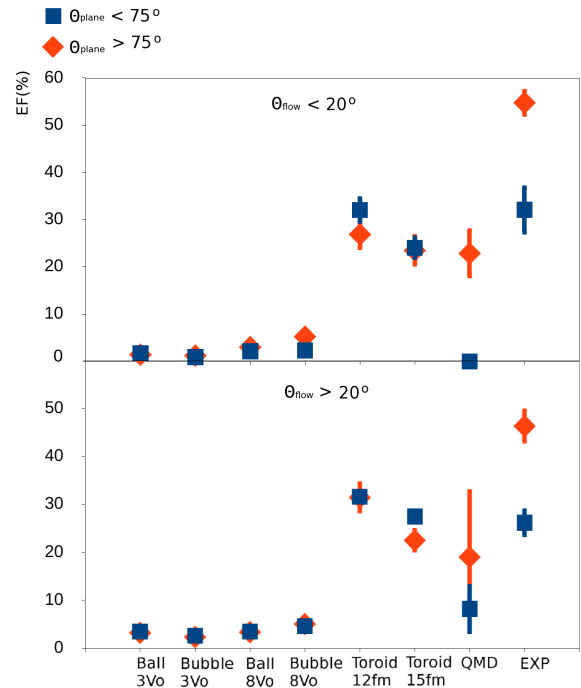


FIG. 12: (color online) The EF values for different windows of θ_{plane} and θ_{flow} . The presented results were sorted using the condition $Z_{frag} \geq 10$.

Efficiency factor (%)

| Configuration | $Z_{frag} \geq 3$ | $Z_{frag} \geq 10$ | $Z_{frag} \geq 15$ | $Z_{frag} \geq 20$ |
|---------------|-------------------|--------------------|--------------------|--------------------|
| Ball $3V_0$ | 3.3 ± 0.2 | 3.5 ± 0.2 | 3.5 ± 0.2 | 3.5 ± 0.2 |
| Bubble $3V_0$ | 2.4 ± 0.2 | 2.6 ± 0.2 | 2.7 ± 0.2 | 2.7 ± 0.2 |
| Ball $8V_0$ | 3.2 ± 0.2 | 3.5 ± 0.2 | 3.5 ± 0.2 | 3.5 ± 0.2 |
| Bubble $8V_0$ | 3.9 ± 0.2 | 4.6 ± 0.2 | 4.7 ± 0.2 | 4.7 ± 0.2 |
| Toroid 12 fm | 29.7 ± 0.6 | 31.6 ± 0.6 | 31.8 ± 0.6 | 31.9 ± 0.6 |
| Toroid 15 fm | 25.2 ± 0.5 | 27.5 ± 0.5 | 27.7 ± 0.5 | 27.8 ± 0.5 |
| QMD | 13.7 ± 3.4 | 8.2 ± 4.7 | 6.3 ± 5.5 | N/A |
| data | 27.1 ± 0.7 | 26.2 ± 2.5 | 26.2 ± 4.8 | 21.1 ± 8.0 |

TABLE I: The efficiency factor at incident energy 23 A MeV for four threshold values of the fragment charge for events selected by conditions $\theta_{flow} > 20^\circ$ and $\theta_{plane} < 75^\circ$.

From Table I we notice that the EF values for experimental data are very close to the model predictions for toroidal configurations. This observation may be one of arguments in favor of the formation of toroidal/flat freeze-out configuration created in the Au + Au collisions at 23 A MeV.

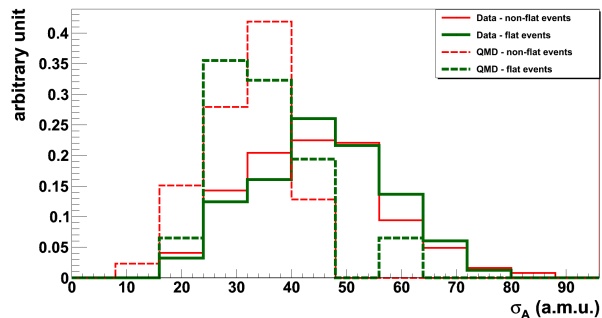


FIG. 13: (color online) The distributions of standard deviation of the fragment mass for non-flat events (red lines) and flat events (green lines) for experimental data (solid lines) and QMD model predictions (dashed lines).

All the distributions presented here are constructed using the condition $Z_{frag} \geq 10$.

B. Other observables

In order to get additional evidence to support the hypothesis that toroidal objects are created the behaviour of other observables was investigated. We consider here for each event separately: (i) standard deviation of fragment mass (σ_A), (ii) relative velocities of fragments pairs (v_{ij}), (iii) mean velocities of fragments as a function of their mass.

First we construct these observables for events selected by conditions $\theta_{flow} > 20^\circ$ and $\theta_{plane} < 75^\circ$, where observation of toroidal freeze-out configurations is expected. The distributions of these observables are generated for flat events selected by condition (7) (thick green histograms) and non-flat events (thin red histograms) selected by condition:

$$\Delta^2 > 0.001 c^2 \text{ and } \delta > 0.05. \quad (8)$$

Comparison of the σ_A distributions (Fig. 13) for flat and non-flat events indicates that in the case of flat events this distribution is slightly shifted to larger values. This observation is in contrast with the expectation that for the flat events the enhanced similarity in the size of fragments should be visible. The corresponding distributions for QMD calculations are similar (dashed lines). Their centroids are shifted to smaller values with respect to experimental data.

In Fig. 14 one observes that the distribution of relative velocities for flat events is shifted to smaller velocities in respect to non-flat events. The corresponding distributions for Toroid 15 fm and Ball $8V_0$ ETNA model predictions show a similar dependence. This observation may indicate that the behaviour of these v_{ij} distributions is insensitive to the shape of the freeze-out configuration.

In Fig. 15 the distributions of mean velocities of fragments as a function of their mass for a flat and non-flat

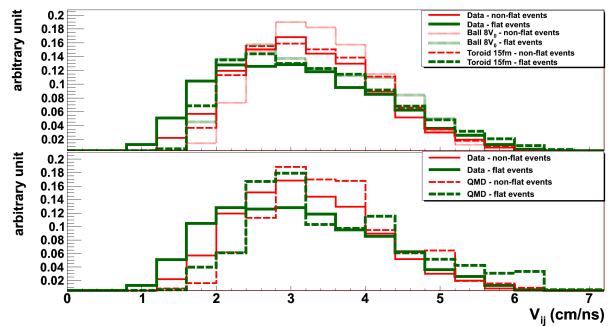


FIG. 14: (color online) The distribution of relative velocities v_{ij} of fragments pairs for non-flat events (red lines) and flat events (green lines) for experimental data (solid lines) compared with: Ball $8V_0$ and Toroid 15 fm (upper panel) and QMD model predictions (bottom panel). All the distributions presented here are constructed using the condition $Z_{frag} \geq 10$.

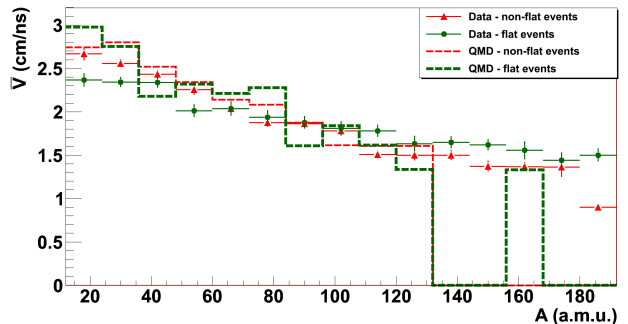


FIG. 15: (color online) The distributions of mean velocities of fragments as a function of their mass for non-flat events (red lines) and flat events (green lines) for experimental data (points with error bars) and QMD model predictions (dashed lines). All the distributions presented here are constructed using the condition $Z_{frag} \geq 10$

events are presented. One can observe that for flat events velocities of fragments decrease weaker with mass comparing to the same dependence for non-flat events. Comparison with same dependences presented for Pb + Ag and Pb + Au systems at 29 A MeV [32] indicates that toroidal configurations may be created for some subclass of flat events.

| Observable | threshold | $\theta_{flow} > 20^\circ$ | $\theta_{flow} > 20^\circ$ | $\theta_{flow} < 20^\circ$ | $\theta_{flow} < 20^\circ$ |
|---------------------|--------------------|-----------------------------|-----------------------------|-----------------------------|-----------------------------|
| | | $\theta_{plane} < 75^\circ$ | $\theta_{plane} > 75^\circ$ | $\theta_{plane} < 75^\circ$ | $\theta_{plane} > 75^\circ$ |
| σ_A (a.m.u.) | $Z_{frag} \geq 3$ | 72.09 \pm 0.47 | 71.09 \pm 0.35 | 76.43 \pm 0.52 | 73.33 \pm 0.13 |
| | $Z_{frag} \geq 10$ | 47.01 \pm 1.88 | 47.15 \pm 1.33 | 46.41 \pm 2.68 | 45.06 \pm 0.58 |
| | $Z_{frag} \geq 15$ | 38.31 \pm 2.98 | 38.53 \pm 1.24 | 35.24 \pm 5.11 | 35.58 \pm 0.98 |
| | $Z_{frag} \geq 20$ | 31.01 \pm 6.68 | 31.10 \pm 2.60 | 25.15 \pm 5.15 | 27.17 \pm 1.59 |
| | $Z_{frag} \geq 25$ | 17.51 \pm 5.07 | 18.95 \pm 5.86 | 20.94 \pm 4.82 | 18.50 \pm 2.23 |
| v_{ij} (cm/ns) | $Z_{frag} \geq 3$ | 3.01 \pm 0.01 | 3.17 \pm 0.01 | 3.27 \pm 0.02 | 3.36 \pm 0.01 |
| | $Z_{frag} \geq 10$ | 3.13 \pm 0.05 | 3.30 \pm 0.03 | 3.30 \pm 0.08 | 3.51 \pm 0.02 |
| | $Z_{frag} \geq 15$ | 3.16 \pm 0.08 | 3.27 \pm 0.05 | 3.27 \pm 0.15 | 3.49 \pm 0.04 |
| | $Z_{frag} \geq 20$ | 3.14 \pm 0.24 | 3.25 \pm 0.11 | 3.24 \pm 0.52 | 3.50 \pm 0.06 |
| | $Z_{frag} \geq 25$ | 2.98 \pm 0.31 | 3.28 \pm 0.33 | 3.26 \pm 0.81 | 3.46 \pm 0.13 |

TABLE II: The mean values of mass standard deviation of the fragments, and of relative velocities v_{ij} of fragments pairs for flat events located in different windows of θ_{flow} and θ_{plane} angles.

Properties of flat events in the region where observation of toroidal freeze-out configurations is expected ($\theta_{flow} > 20^\circ$ and $\theta_{plane} < 75^\circ$) can be also compared with properties of flat events corresponding to other regions of θ_{flow} and θ_{plane} angles. Here the considered regions are the same as presented in Fig. 12. The distributions for σ_A of fragments, and v_{ij} of fragments pairs are presented in Fig. 16 using the condition $Z_{frag} \geq 10$. The mean values of these distributions are listed in Table II. We can notice here that the corresponding mean values of the distribution of σ_A are similar for all θ_{flow} and θ_{plane} windows for a given threshold value of the fragment charge Z_{frag} . Such observation shows us that information carried by σ_A can not be used as an indication of toroidal objects formation. For v_{ij} distributions one observes that the mean values for class of events located outside the reaction plane are smaller in comparison to the case of events located in the reaction plane. The smallest mean values are seen for the region where observation of toroidal freeze-out configurations are expected. This observation may be used as an indication that for events located outside the reaction plane freeze-out configuration is more extended in comparison with that for events located inside reaction plane.

Results obtained for the considered observables suggest that the formation of toroidal configurations can be related to a fraction of flat events tilted with respect to the reaction plane ($\theta_{plane} < 75^\circ$). The probability for these events is much greater than the prediction of the QMD model. The nature of these events should be investigated.

Assuming that the total number of detected events corresponds to 80% of total reaction cross section, the cross section related to creation of flat tilted events located in the region where observation of toroidal freeze-out configurations is expected can be estimated to be equal $17\mu b$.

V. SUMMARY

We presented an analysis of events produced in Au + Au collisions at 23 AMeV. Basic information about data calibration procedure were summarized. The bulk

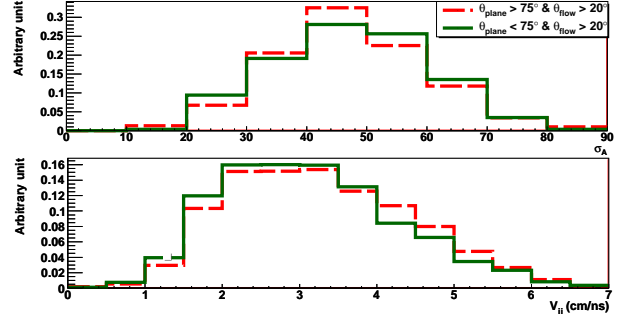


FIG. 16: (color online) The distributions of standard deviation of the fragment mass (upper panel), and the distributions of relative velocities v_{ij} of fragments pairs (bottom panel) for flat events. The red dashed lines corresponds to events located inside the reaction plane and the green solid lines correspond to events located outside the reaction plane. All the distributions presented here are constructed using the condition

$$Z_{frag} \geq 10$$

properties of the experimental data were shown. The experimental data were compared with ETNA and QMD model predictions. Proximity of efficiency factor values for experimental data and toroidal freeze-out configurations may be used as an indication of the formation of an exotic freeze-out configuration. The juxtaposition of the standard deviation of fragment mass values for events located outside and inside the reaction plane are not suggestive of a toroidal freeze-out configuration. Comparison of distributions of relative velocities for event with different orientation in respect to reaction plane gives evidence that the freeze-out configuration is more extended for events located outside reaction plane. The behavior of mean velocities of fragments as a function of their mass for flat and non-flat events gives an indication that toroidal configuration may be created for some subclass of flat events.

The probability of appearance of these flat events is much greater than the prediction of the QMD model. The nature of flat events tilted with respect to the reaction plane should be investigated.

VI. ACKNOWLEDGMENTS

Special thanks are due the INFN-LNS operating crew for providing an excellent beam. This work has been partly supported by the National Science Centre of Poland (grant N N202 180638, 2013/09/N/ST2/04383).

-
- [1] J.A.Wheeler, Nucleonic Notebook, (1950) unpublished.
- [2] P.J.Siemens, H.Bethe, Phys. Rev.Lett. **18**, 704 (1967).
- [3] C.Y.Wong, Phys. Rev. Lett. **55**, 1973 (1985).
- [4] L.G.Moretto *et al.*, Phys. Rev. Lett. **78**, 824 (1997).
- [5] K.Dietrich and K.Pomorski, Phys. Rev. Lett. **80**, 37 (1998).
- [6] J.F.Berger *et al.*, Nucl. Phys. **A685**, 1 (2001).
- [7] J.Decharge *et al.*, Nucl. Phys. **A716**, 55 (2003).
- [8] M.Warda, Int. J. Mod. Phys. **E16**, 452 (2007).
- [9] A.Staszczak and C.Y.Wong, Acta Phys. Pol. **B40**, 753 (2009).
- [10] A.Sochocka *et al.*, Int. J. of Mod. Phys. **E17**, 190 (2008).
- [11] A.Sochocka *et al.*, Acta Phys. Pol. **B39**, 405 (2008).
- [12] J.Tian *et al.*, Phys. Rev. **C77**, 064603 (2008).
- [13] Kuo-Long Pan *et al.*, Phys. Rev. **E80**, 036301 (2009).
- [14] A. Pagano, Nucl. Phys. News **22**, 28 (2012), and ref. therein.
- [15] E.De Filippo and A.Pagano, Eur. Phys. Jour. **A50**, 32 (2014).
- [16] A.Sochocka *et al.*, Acta Phys. Pol. **B40**, 747 (2009).
- [17] A.Sochocka, PhD Thesis, Krakow, 2009.
- [18] I. Skwira-Chalot *et al.*, Phys. Rev. Lett. **101**, 262701 (2008).
- [19] J.Wilczyński *et al.*, Phys. Rev. **C81**, 024605 (2010).
- [20] J.Wilczyński *et al.*, Phys. Rev. **C81**, 067604 (2010).
- [21] T.Cap *et al.*, Phys. Scr. **89**, 054005 (2014).
- [22] G. Tăbăcaru *et al.*, Nucl. Instr. Meth. **A428**, 379 (1999).
- [23] G.Pasquali *et al.*, Nucl. Instr. Meth. **A405**, 39 (1998).
- [24] K.Summerer *et al.*, Phys. Rev. **C42**, 2546 (1990).
- [25] K.Summerer *et al.*, Phys. Rev. **C61**, 034607 (2000).
- [26] K.Summerer, Phys. Rev. **C86**, 014601 (2012).
- [27] G. Lanzalone, LNS Activity Report 2004, p. 125.
- [28] T. Cap *et al.*, Phys. Scr. T154, 014007 (2013).
- [29] J.Aichelin, Phys. Rep. **202**, 233 (1991).
- [30] J.Lukasik and Z.Majka, Acta Phys. Pol. **B24**, 1959 (1993).
- [31] J.Cugnon and D.L'Hote, Nucl. Phys. **A397**, 519 (1983).
- [32] B.Jouault *et al.*, Nucl. Phys. **A615**, 82 (1997).